Research Square

Preprints are preliminary reports that have not undergone peer review.
They should not be considered conclusive, used to inform clinical practice,
or referenced by the media as validated information.

Distance Estimates to Five Bok Globules Using Gaia DR3 Parallaxes and Near-Infrared Photometry: Validation with 3D Dust Maps

Rajat Subhra Paul
Karimganj College
Himadri Sekhar Das
himadri.sekhar.das@aus.ac.in
Assam University

Research Article

Keywords: Dark clouds, Distance determination, Extinction, Near-infrared photometry, Bok globules, Gaia parallaxes

Posted Date: April 7th, 2026

DOI: https://doi.org/10.21203/rs.3.rs-9107076/v1

License: This work is licensed under a Creative Commons Attribution 4.0 International License.
Read Full License

Additional Declarations: No competing interests reported.

Version of Record: A version of this preprint was published at Astrophysics and Space Science on July 29th, 2026. See the published version at https://doi.org/10.1007/s10509-026-04608-x.

Distance Estimates to Five Bok Globules Using Gaia DR3 Parallaxes and Near-Infrared Photometry: Validation with 3D Dust Maps

Rajat Subhra Paul · Himadri Sekhar Das

Received: date / Accepted: date

Abstract Accurate distances to small, opaque Bok globules are difficult to obtain due to their compact sizes and lack of embedded standard candles. We estimate distances to five globules—CB4, CB24, CB56, CB60, and CB188—using a near-infrared (NIR) extinction technique applied to 2MASS photometry, combined with stellar distances from *Gaia* DR3 parallaxes. Extinction–distance profiles reveal distinct rises marking each cloud, yielding median distances of 766 pc (CB4), 354 pc (CB24), 483 pc (CB56), 1143 pc (CB60), and 926 pc (CB188). Weighted-mean values agree within 8.5%, confirming internal consistency. Independent validation with Bayestar19 3D dust maps supports the CB4 and CB188 results. These refined distances enable reliable determinations of cloud masses, densities, and star-formation efficiencies, including the first robust measurement for CB56 and a revised upward distance for CB188.

Keywords Dark clouds · Distance determination · Extinction · Near-infrared photometry · Bok globules · Gaia parallaxes

1 Introduction

Bok globules are small, nearly isolated molecular clouds with typical diameters of 0.1–2 pc and masses between 2 and 100 $M_{\odot}$ (Bok, 1977). These objects serve as ideal laboratories for investigating early-stage star formation, protostellar collapse, and magnetic field interactions (Clemens et al., 1991), while remaining relatively uncontaminated by nearby stellar clusters. Evidence of ongoing low-mass star formation includes bipolar molecular outflows (Yun & Clemens, 1994a), submillimeter continuum emission, and infrared colors consistent with Class 0 or Class I protostars (Yun & Clemens, 1994b; Launhardt et al., 1997).

R. S. Paul
Department of Physics, Karimganj College, Sribhumi 788711, India
E-mail: apurajatsubhra@gmail.com

H. S. Das
Department of Physics, Assam University, Silchar 788011, India
E-mail: himadri.sekhar.das@aus.ac.in

Accurate distance measurements are fundamental to deriving key physical parameters such as mass, size, density, and luminosities of embedded young stellar objects (YSOs) (Clemens et al., 1991; Yun & Clemens, 1990). Without precise distances, it is impossible to distinguish genuine cloud properties from apparent differences arising from projection effects or distance uncertainties. Distance determination has evolved from early star count methods (Wolf, 1923; Bok & Bok, 1941) and bracketing techniques (Hobbs et al., 1986) to modern approaches utilizing broadband photometry (Peterson & Clemens, 1998; Hearty et al., 2000), extinction mapping (Lombardi et al., 2008), and astrometric missions. The *Gaia* mission has provided unprecedented parallax precision (*Gaia* Collaboration, 2016, 2022), enabling revolutionary improvements in cloud distance determinations.

The near-infrared (NIR) photometric technique, successfully applied by Maheswar et al. (2010) using 2MASS (J–H) and (H–K_S) color indices of main-sequence stars (A0–K7), has emerged as a powerful tool for measuring distances to isolated clouds. This approach was successfully applied by Eswaraiah et al. (2013) to LDN 1570, Barman & Das (2015) to CB4, and Das et al. (2015) to six Bok globules.

While these NIR photometric techniques have proven successful for several isolated clouds, their application remains limited, leaving many Bok globules with poorly constrained or entirely unknown distances. Despite their significance as pristine laboratories of low-mass star formation, many Bok globules still lack precise distance estimates, limiting accurate determinations of their physical properties. Building on the methodology of Choudhury et al. (2019), we present improved distances for five Bok globules—CB4, CB24, CB56, CB60, and CB188. The work pursues three primary goals: (1) to exploit the astrometric accuracy of *Gaia* DR3 to refine distance estimates and resolve literature discrepancies by factors of 2–3; (2) to provide the first reliable distance measurement for CB56; and (3) to introduce a dual-metric framework that combines weighted-mean and median-based distance estimations, offering enhanced statistical robustness and resistance to outliers for sparsely sampled fields ($N = 16$–103 stars).

Our analysis employs three layers of validation: internal consistency checks (showing $< 10\%$ disagreement between the two estimation methods for all clouds), extinction-break detection to pinpoint the physical cloud location, and independent cross-verification using the `Bayestar19` 3D dust extinction maps of Green et al. (2019) for CB4 and CB188. The resulting distances, with uncertainties of ~ 1–3%, enable reliable determinations of mass and luminosity (both scaling as d^2). These refined measurements have substantial implications, including a revised distance upward by a factor of ~ 3.5 for CB188 and establishing the first robust distance baseline for future studies of CB56.

2 Object Identification

We have selected five Bok globules spanning a range of cloud properties and evolutionary stages. Brief descriptions are provided below; their comprehensive observational properties are listed in Table 1.

2.1 Individual Cloud Descriptions

CB4 is a small, spherical, and relatively isolated dark globule with an ambiguous distance in the literature (200–600 pc; Dickman & Clemens (1983), Launhardt et al. (2010)). Despite its compact appearance and low temperature ($\sim$ 7 K), CB4 lacks embedded sources brighter than the IRAS 100 μm limit and exhibits cirrus-like characteristics. Its well-ordered magnetic field (position angle 71°; Sen et al. (2005)) appears aligned with the Galactic field, making it a quiescent but scientifically valuable target.

CB24 is a small, spherical Bok globule detected at $l = 155.76°$, $b = 5.9°$ with CO $J = 1 \rightarrow 0$ velocity $V_{\rm LSR} = 4.6$ km s^{-1} and a distance of 293 $\pm$ 54 pc from our prior study (Das et al., 2015). Unlike many globules, CB24 lacks associated IRAS sources and exhibits exceptionally low column densities, likely representing a genuine starless core in an early evolutionary stage characterized by minimal star formation activity. No embedded protostars have been detected toward this cloud.

CB56 is an asymmetrical, dense cloud at $l = 237.93°$, $b = -6.46°$ with a major-axis position angle of 170°, for which no distance estimate has been previously published. Two IRAS point sources (07125–2503 and 07125–2507) are associated with it, suggesting ongoing or recent star formation activity. The cloud exhibits well-aligned polarization vectors ($p_{\rm av} = 1.08\%$, $\theta_{\rm av} = 150.94°$), indicative of organized magnetic fields and grain alignment, making it an interesting target for studying the relationship between magnetic fields and cloud fragmentation.

CB60 is a B-type cloud with an anomalously warm temperature and three associated IRAS point sources (08026–3122, 08029–3118, 08022–3155). Its polarization vectors show a local magnetic-field alignment distinct from the Galactic plane ($p_{\rm av} = 1.3\%$, $\theta_{\rm av} = 155.15°$), indicating a possible decoupling from large-scale Galactic fields.

CB188 is a low-mass, spherical Bok globule in Aquila at a distance of approximately 260 pc (Das et al., 2015), associated with the Lindblad loop. It harbors a single Class I protostar (IRAS 19179+1129) and represents a gravitationally unstable core with a total mass of $\sim$ 7 $M_\odot$ and a central density of $\sim 1 \times 10^5$ cm^{-3} (Kandori et al., 2005). Its Local Standard of Rest velocity ($\sim$ 7 km s^{-1}) is consistent with that of the surrounding molecular complexes.

3 Data and Methods

3.1 Near-Infrared Photometric Technique

3.1.1 Principle and Historical Development

The NIR photometric technique exploits wavelength-dependent extinction by interstellar dust to derive stellar parameters and extinction values. By comparing observed NIR colours of stars with their intrinsic main-sequence colours, we derive visual extinction (A_V) along each line of sight; sharp increases in A_V with distance mark cloud locations. Maheswar et al. (2010) developed this approach using 2MASS $(J-H)$ and $(H-K_S)$ colour indices of main-sequence stars (A0–K7), which was subsequently refined by Choudhury et al. (2019) through integration

Table 1 Physical and Observational Properties of Selected Bok Globules

Property	CB4	CB24	CB56	CB60	CB188
Positions and Coordinates					
RA (J2000)	00:39:03	04:58:30	07:14:36	08:04:36	19:20:17
Dec (J2000)	+52:51:29	+52:15:41	–25:08:54	–31:30:47	+11:36:12
Galactic l (deg)	121.03	155.76	237.93	248.89	46.53
Galactic b (deg)	–9.97	5.91	–6.46	–0.01	–1.02
Cloud Properties					
Cloud Type	Quiescent	Starless	Dense	B-type, Active	Low-mass, Active
IRAS Sources	1 @ 100 μm	None	2 sources	3 sources	1 YSO
Temperature	$\sim$ 7 K	...	...	Warm	...
Magnetic Field Properties					
Mag. Field Angle (deg)	71 (ord.)	...	150.94	155.15	...
Polarization $p_{\rm av}$ (%)	...	...	1.08 ± 0.56	1.30 ± 0.94	...
Physical Parameters					
Mass ($M_\odot$)	1.6	...	...	...	$\sim$7
$V_{\rm LSR}$ (km s^{-1})	–12	4.6	...	...	$\sim$7
Literature Distance					
Distance (pc)	350±150[a], 459±85[b]	293±54	...	1500	262±49
Reference	[a]DC (1983), [b]BD (2015)	D(2015)	...	L(1997)	D(2015)

Ellipses (...) indicate data not available in the literature. DC (1983), BD (2015), L(1997) and D(2015) correspond to Dickman & Clemens (1983), Barman & Das (2015), Launhardt et al. (1997), and Das et al. (2015), respectively.

with *Gaia* parallax data. Our distance estimation procedure follows this same NIR extinction technique, from which cloud distances are extracted from extinction–distance profiles and subsequently validated using the Bayestar19 3D dust map (Green et al., 2019).

3.1.2 Mathematical Framework

Step 1: Distance from *Gaia* DR3 Parallax

Stellar distances are obtained directly from *Gaia* DR3 parallaxes:

$$d\ (\mathrm{pc}) = \frac{1000}{\pi} \tag{1}$$

where π is the parallax in arcseconds.

Step 2: Observed Colors from 2MASS

For each star, observed magnitudes (J, H, K_S) from 2MASS yield observed colors:

$$(J-H)_{\rm obs} = m_J - m_H \tag{2}$$

$$(H-K_S)_{\rm obs} = m_H - m_{K_S} \tag{3}$$

Step 3: Iterative Extinction and Spectral Type Determination

We iteratively determine extinction A_V and spectral type through the following procedure:

(a) Assume trial extinction value A_V (ranging from 0.1 to 20 mag in 0.1 mag steps)

(b) Apply Rieke & Lebofsky (1985) reddening law to compute extinction in each band:

$$A_J = 0.282 \times A_V \tag{4}$$
$$A_H = 0.175 \times A_V \tag{5}$$
$$A_{K_S} = 0.112 \times A_V \tag{6}$$

(c) Calculate dereddened (intrinsic) colors:

$$(J-H)_0 = (J-H)_{\rm obs} - (A_J - A_H) = (J-H)_{\rm obs} - 0.107 \times A_V \tag{7}$$
$$(H-K_S)_0 = (H-K_S)_{\rm obs} - (A_H - A_{K_S}) = (H-K_S)_{\rm obs} - 0.063 \times A_V \tag{8}$$

(d) Determine spectral type by minimizing χ^2 difference between observed dereddened colors and intrinsic main-sequence colors (A0–K7) from Cox et al. (2000) calibrations:

$$\chi^2 = \frac{[(J-H)_{0,\rm obs} - (J-H)_{0,\rm MS}]^2}{\sigma^2_{J-H}} + \frac{[(H-K_S)_{0,\rm obs} - (H-K_S)_{0,\rm MS}]^2}{\sigma^2_{H-K_S}} \tag{9}$$

(e) For the best-fit spectral type, obtain absolute magnitude M_{K_S} from main-sequence relations.

(f) Compare calculated distance $d_{\rm calc}$ from the extinction-corrected distance modulus:

$$d_{\rm calc} = 10^{(m_{K_S} - A_{K_S} - M_{K_S} + 5)/5} \text{ pc} \tag{10}$$

where $A_{K_S} = 0.112 \times A_V$ (Eq. 6). Compare $d_{\rm calc}$ with *Gaia* distance $d_{\rm Gaia}$. Iterate A_V until convergence ($|d_{\rm calc} - d_{\rm Gaia}|$ minimized).

Step 4: Final Extinction Value

The converged A_V represents the total visual extinction along the line of sight to each star at its *Gaia*-determined distance.

3.1.3 Critical Distinction: NIR Photometry vs Optical Astrometry

Important Methodological Note: This technique employs a dual-data approach that is critical to its success in studying moderately extincted clouds. We use *near-infrared* (NIR) photometry from 2MASS ($J = 1.25$ μm, $H = 1.65$ μm, $K_s = 2.17$ μm) to measure extinction *through* the clouds, not optical photometry. NIR wavelengths experience significantly lower extinction than optical wavelengths, with the extinction in the NIR bands being approximately 10 times lower than visual extinction.

Specifically, from the Rieke & Lebofsky (1985) reddening law (Eqs. 4–6):

- $A_J/A_V = 0.282$ (J-band extinction is 28% of visual)
- $A_H/A_V = 0.175$ (H-band extinction is 18% of visual)
- $A_{K_s}/A_V = 0.112$ (Ks-band extinction is 11% of visual)

This means a cloud with $A_V = 20$ mag (optically opaque) has only $A_J \approx 5.6$ mag, $A_H \approx 3.5$ mag, and $A_{K_s} \approx 2.2$ mag in the NIR bands—well within 2MASS detection limits for background stars.

Gaia DR3 parallaxes are used *only* for measuring distances to field stars via trigonometric parallax (Eq. 1), not for obtaining photometry through the cloud

itself. This separation of functions—NIR photometry for extinction measurement + optical astrometry for distance determination—is what enables the method to work effectively for clouds where optical photometry would be severely compromised by extinction.

The method is most reliable for clouds with $A_{V,\max} \lesssim 15$ mag, corresponding to $A_J \lesssim 4.2$ mag, which still allows sufficient 2MASS background star detection for constructing extinction-distance profiles. All five Bok globules in this study satisfy this criterion (see Section 3.1.4).

3.1.4 Data Selection Criteria

We obtained near-infrared photometry for stars within a $30' \times 30'$ field around each globule from the 2MASS Point Source Catalog (Cutri et al., 2003). Selected sources met the following criteria:

(a) **Quality flags**: Quality flag (Qflag) = 'AAA' in all three filters (J, H, K_S), indicating high signal-to-noise ratio (SNR > 10) and reliable detections.
(b) **Photometric uncertainties**: Uncertainties ≤ 0.045 mag in all three filters, ensuring accurate color indices.
(c) **Spectral type range**: $J - K_S \leq 0.75$ to exclude unreddened M-type stars. This criterion is critical because unreddened M-type dwarfs occupy the same reddening vector as reddened A0–K7 dwarfs in the $(J - H, H - K_S)$ color diagram (Maheswar et al., 2010), potentially introducing systematic biases in extinction determination. By restricting to $J - K_S \leq 0.75$, we exclude the vast majority of unreddened M-type stars while retaining reddened early- to mid-type stars most sensitive to extinction variations.

Parallax data were obtained from the *Gaia* DR3 catalog (*Gaia* Collaboration, 2016, 2022) with the requirement that parallax $\pi > 0$ (physically meaningful distances).

3.2 Data Processing Pipeline

Our analysis follows a systematic procedure:

1. **Source Selection**: Extract all 2MASS sources in the $30' \times 30'$ field meeting quality criteria (a)-(c) from Section 3, subsection 3.1.3.
2. **Parallax Cross-Matching**: Match 2MASS sources with *Gaia* DR3 parallaxes within $1''$ angular separation; calculate distances d (pc) $= 1000/\pi$ (parallax in arcseconds).
3. **Extinction Calculation**: For each star, calculate visual extinction A_V by iteratively fitting trial values (0.1 to 20 mag in 0.1 mag steps), dereddening colors, determining best-fit spectral type by minimizing χ^2 between observed dereddened colors and main-sequence standards, and converging when photometric distance matches *Gaia* distance.
4. **Distance Determination**: Apply the dual-metric approach combining weighted mean calculation with median distance estimation, as detailed in Section 4.

5. **Validation**: Cross-match results with *Gaia* DR3 uncertainties to ensure parallax quality. Verify agreement between weighted mean and median distances (target: $< 10\%$ difference) and confirm consistent extinction signatures indicative of genuine cloud structure.

3.3 Extinction Uncertainty Propagation

The uncertainty in A_V for each star arises from multiple sources: photometric measurement errors in 2MASS colors, uncertainties in spectral type determination, and systematic uncertainties in the reddening law coefficients. We propagate these uncertainties through the dereddening process to obtain the total A_V uncertainty for each star.

The photometric uncertainties from 2MASS (σ_{J-H} and σ_{H-K_S}) propagate through the color-extinction relations with different sensitivities in each color index. The spectral type fitting procedure introduces additional uncertainty, typically equivalent to $\sim$ 0.5–1 spectral subclass uncertainty, which translates to approximately 0.1–0.2 mag in A_V. Furthermore, systematic uncertainties in the Rieke & Lebofsky (1985) reddening law coefficients contribute approximately 5–10% of the derived A_V value.

These individual uncertainty components are combined in quadrature to yield the total extinction uncertainty σ_{A_V} for each star. This comprehensive error budget ensures that systematic errors in spectral type determination or reddening law assumptions do not dominate the extinction measurement uncertainty.

For distance determination, we apply a two-tier selection threshold based on extinction significance:

- **Standard threshold**: $A_V - \sigma_{A_V} > 0.4$ mag, corresponding to $> 4\sigma$ detection significance ($> 99.99\%$ confidence), ensuring highly reliable extinction measurements. This threshold is applied to CB24, CB56, CB60, and CB188.
- **Relaxed threshold (low-extinction clouds only)**: $A_V - \sigma_{A_V} > 0.2$ mag for clouds where no stars meet the strict criterion, preventing complete sample elimination while maintaining reasonable detection confidence ($> 2\sigma$). This relaxed criterion is applied only to CB4 due to its low optical depth and substantial foreground extinction.

This approach ensures that only stars with robust, statistically significant extinction measurements contribute to the cloud distance determination, minimizing contamination from foreground stars or measurement artifacts.

3.4 Sample Selection and Cloud Morphology

The five Bok globules analyzed in this study are shown in Figures 1–5, where each panel displays a Digital Sky Survey (DSS) R-band image of the respective globule along with the selected 2MASS field stars used in the distance determination. The DSS images clearly reveal the morphology and projected structure of each cloud, providing visual confirmation of their compact, isolated nature. The field stars shown in these figures were selected following the comprehensive quality criteria specified in Section 3, subsection 3.1.3.

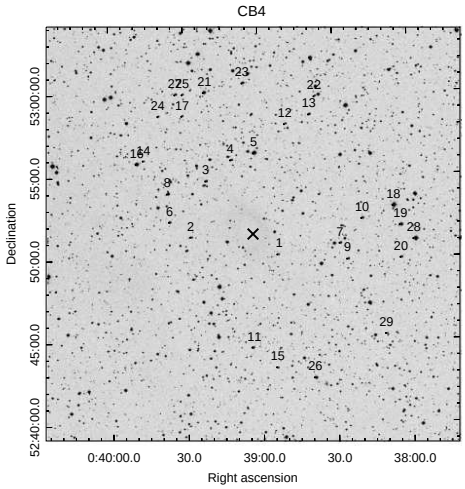


Fig. 1 DSS R-band image of Bok Globule CB4 showing the 29 selected 2MASS field stars used in the analysis, chosen according to the criteria described in Section 3 (subsection 3.1.4).

CB4 (Figure 1, 29 selected stars): The globule appears as a dark, compact, nearly spherical structure with clear boundaries against the background stellar field.

CB24 (Figure 2, 29 selected stars): This globule exhibits similar spherical morphology to CB4, but with slightly less contrast against the background. The selected stars provide good spatial coverage for extinction analysis.

CB56 (Figure 3, 103 selected stars): Unlike CB4 and CB24, CB56 exhibits asymmetrical morphology with an irregular boundary, consistent with its dense, structured appearance. The substantial number of available stars enables robust statistical analysis.

CB60 (Figure 4, 40 selected stars): This globule appears compact but exhibits patchy structure characteristic of B-type clouds with active star formation.

CB188 (Figure 5, 16 selected stars): Despite the smallest sample size, this number is adequate for distance determination. The cloud's spherical morphology and compact structure are clearly evident.

4 Distance Estimation Method

4.1 Data Sources and Extinction Measurements

Stellar distances and visual extinctions A_V were computed as described in Section 3. To focus on stars in the immediate vicinity of each cloud, we defined a maximum projected radial distance $r_{\max}$ from the cloud center, excluding stars projected beyond this radius. The $r_{\max}$ values for each cloud (Table 2) were chosen to encompass the main cloud structure visible in DSS images while excluding unrelated field stars. Parallax uncertainties for stars in the *Gaia* DR3 catalog typically

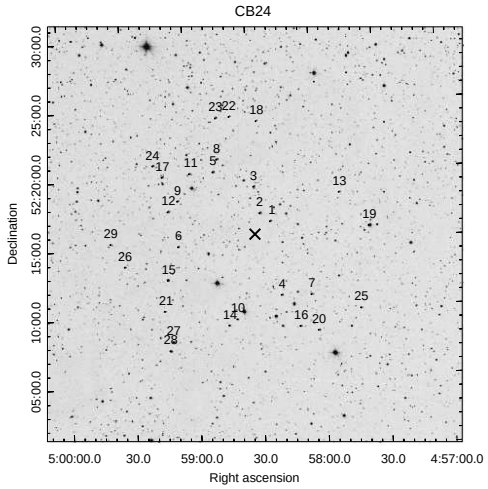


Fig. 2 Same as Figure 1 but for CB24 (29 selected stars).

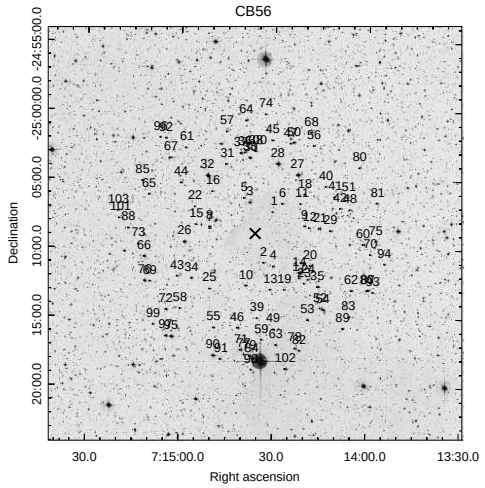


Fig. 3 Same as Figure 1 but for CB56 (103 selected stars).

range from ~ 0.1–1 mas for the magnitude ranges considered here ($J \sim 10$–14), corresponding to relative distance uncertainties of ~ 1–10% at distances 300–1500 pc.

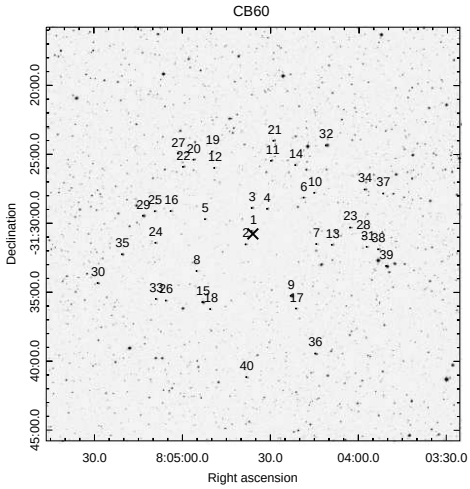


Fig. 4 Same as Figure 1 but for CB60 (40 selected stars).

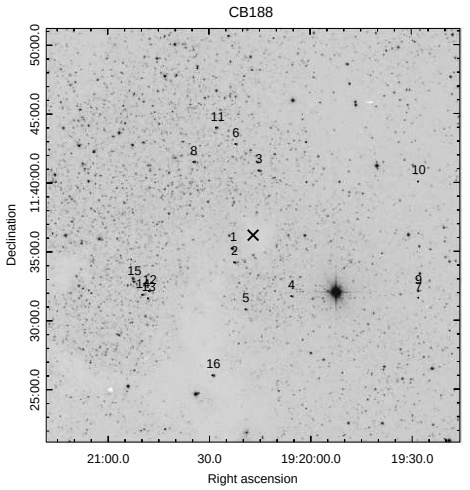


Fig. 5 Same as Figure 1 but for CB188 (16 selected stars).

4.2 Selection Criteria

To ensure that distance estimates are based on stars with reliable extinction measurements and well-determined parallaxes, we applied the following selection criteria:

4.2.1 Standard Selection Criteria (CB24, CB56, CB60, CB188)

(i) $A_V - \sigma_{A_V} > 0.4$: This requires that the extinction signal exceeds the noise by $\geq 4\sigma$, ensuring detections are highly significant ($> 99.99\%$ confidence). This threshold preferentially selects moderately to heavily reddened stars where extinction determination is most reliable.

(ii) $D/\sigma_D > 3$: Distance measurement uncertainty should be $\leq 33\%$ of the distance itself. For *Gaia* DR3 parallaxes, this typically restricts the sample to $V < 14$ mag or parallax uncertainties $\sigma_\pi < 0.3$ mas, ensuring reliable trigonometric distances.

(iii) $A_V/\sigma_{A_V} > 1.5$: Extinction-to-noise ratio must exceed 1.5, providing an additional buffer against systematic errors in spectral type determination or dust model assumptions.

4.2.2 Relaxed Criteria (CB4: $A_V - \sigma_{A_V} > 0.2$, $D/\sigma_D > 3$, $A_V/\sigma_{A_V} > 1.2$)

Application of standard criteria to CB4 yielded only 8 candidate stars, which is at the lower limit for reliable distance determination via weighted averaging. Analysis of the extinction-distance plot for CB4 revealed that the cloud's relatively low optical depth ($A_{V,\max} \sim 3$–4 mag) combined with its substantial foreground column density makes stars meeting stringent criteria rare. Consequently, we relaxed criteria to $A_V - \sigma_{A_V} > 0.2$ (detection at $> 2\sigma$), retaining $A_V/\sigma_{A_V} > 1.2$ for reasonable reliability. This adjustment increased the sample to 11 stars, enabling robust weighted averaging. We note that while CB4 distances should be interpreted with slightly higher uncertainty due to relaxed criteria, the results remain physically meaningful and comparable to independent estimates (Section 6).

4.3 Distance Determination Procedure

Our distance determination employs a systematic five-step approach that combines weighted mean calculation with median distance estimation and extinction break analysis.

4.3.1 Step 1: Weighted Mean Distance (Reference Point)

For each cloud, we calculated the weighted mean distance using inverse-variance weighting:

$$\langle d \rangle = \frac{\sum_i w_i d_i}{\sum_i w_i} \tag{11}$$

$$w_i = \frac{1}{\sigma_{d,i}^2} \tag{12}$$

$$\sigma_{\langle d \rangle} = \frac{1}{\sqrt{\sum_i w_i}} \tag{13}$$

where d_i is the distance of the i-th star, w_i are weights inversely proportional to squared distance uncertainties, and $\sigma_{d,i}$ is the uncertainty in stellar distance. This weighting scheme emphasizes high-precision measurements and provides formal uncertainty estimates. The weighted mean $\langle d \rangle$ serves as an important reference point for subsequent extinction break analysis.

4.3.2 Step 2: Extinction Break Analysis and Distance Limits

The visual extinction (A_V) is plotted as a function of heliocentric distance for all selected stars (Figures 6–10). A characteristic sharp transition in extinction marks the cloud location. The analysis proceeds as follows:

1. **Reference Point**: Use $\langle d \rangle$ as the reference heliocentric distance.
2. **Extinction Distribution Analysis**: Examine the distribution of extinction values relative to $\langle d \rangle$:
   - Stars at distances $< \langle d \rangle$ typically show lower extinction (foreground ISM)
   - Stars at distances near/within the cloud show sharp extinction increase
   - Stars at distances $> \langle d \rangle$ show high extinction or plateau
3. **Identify Extinction Break Location**: Locate the distance at which extinction rises most sharply, indicating the cloud's front edge (transition zone). This break location may occur before, at, or after $\langle d \rangle$.
4. **Establish Distance Limits**: Based on extinction distribution:
   - **Case A (Extinction break $<$ weighted mean)**: High-extinction stars found primarily at $d < \langle d \rangle$
     - Lower limit: d_{lower} = extinction break distance
     - Upper limit: $d_{\text{upper}} = \langle d \rangle$
   - **Case B (Extinction break $>$ weighted mean)**: High-extinction stars found primarily at $d > \langle d \rangle$
     - Lower limit: $d_{\text{lower}} = \langle d \rangle$
     - Upper limit: d_{upper} = extinction break distance
5. **Cloud Distance Range**: The true cloud distance lies between d_{lower} and d_{upper}, with both limits informed by the extinction-distance relationship.

4.3.3 Step 3: Median Distance as Primary Estimator

From the population of selected stellar distances, we calculate the median distance d_{median} as the primary distance estimator (Eq. 14). The median is preferred over the weighted mean as the primary result because it is robust against outliers, makes no assumption of Gaussian statistics (ideal for small samples of $N = 16$–103 stars), and is validated by the weighted mean: agreement between the two confirms reliability. The weighted mean $\langle d \rangle$ serves as an important reference point and provides formal uncertainty estimates for cross-validation.

$$d_{\text{median}} = \begin{cases} d_{(N+1)/2} & \text{for odd } N \\ \dfrac{d_{N/2} + d_{(N/2+1)}}{2} & \text{for even } N \end{cases} \tag{14}$$

where N is the number of selected stars and $d_{(i)}$ represents the i-th distance in sorted order.

4.3.4 Step 4: Uncertainty Quantification

The interquartile range (IQR) provides a non-parametric uncertainty estimate:

$$\text{IQR} = Q_3 - Q_1 \tag{15}$$

where Q_1 (first quartile, 25th percentile) and Q_3 (third quartile, 75th percentile) represent the distances below and above which 25% and 75% of the stellar distances fall, respectively. The IQR quantifies the spread in individual stellar distance measurements and does not depend on formal error propagation.

4.3.5 Step 5: Validation Through Agreement Assessment

Agreement between weighted mean and median is quantified as:

$$\text{Agreement (\%)} = \frac{|\langle d \rangle - d_{\text{median}}|}{d_{\text{median}}} \times 100\% \tag{16}$$

Agreement $< 10\%$ indicates good consistency; $> 20\%$ would suggest a multimodal distribution requiring investigation. All five clouds in this study achieve $< 8.5\%$ agreement, confirming that neither method is systematically biased.

5 Results

5.1 Distance Determination Sample Properties

The properties of stars used in the distance determination for each cloud are summarized in Table 2. The sample sizes for standard criteria ranged from 16 stars (CB188) to 103 stars (CB56), providing statistically robust distance estimates for all clouds. CB4, requiring relaxed criteria as discussed in Section 4, was based on 29 stars meeting the modified threshold.

5.2 Extinction-Distance Analysis and Cloud Location Identification

The visual extinction (A_V) determined for all field stars is plotted as a function of both projected radial distance from the cloud center and heliocentric distance in Figures 6–10, following the procedure of Section 4. Selected stars meeting stringent criteria are highlighted in black, while non-selected stars are shown as gray circles. Yellow shaded regions indicate the probable cloud distance interval(s) identified from extinction break and 3D dust map comparisons. For all five clouds, the extinction-distance plots display clear transitions marking cloud locations, with median distances agreeing well with weighted mean distances ($< 8.5\%$ difference), validating our dual-metric approach.

5.3 CB4: Extinction Structure and Distance Determination

Figure 6 shows the extinction profile of CB4. The cloud exhibits confined structure within $r_{\text{max}} = 7.0$ arcmin (panel i), with a sharp extinction rise in the range 763–769 pc (panel ii). The weighted mean distance ($\langle d \rangle = 769.4 \pm 8.3$ pc) coincides with the extinction break, indicating excellent convergence between methods. The median distance ($d_{\text{median}} = 766$ pc) falls at the center of this transition zone, with only 0.4% difference from the weighted mean—the best agreement among all five clouds. The yellow shaded region (763–769 pc) from the 3D dust extinction map of Green et al. (2019) independently confirms our distance determination, providing strong external validation.

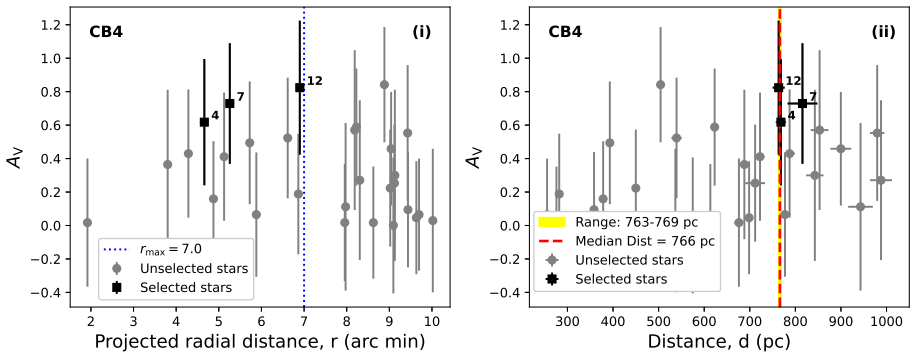


Fig. 6 Extinction analysis for CB4. **(i)** Extinction (A_V) as a function of projected radial distance from the cloud center. The dotted vertical line marks $r_{\rm max} = 7.0$ arcmin, indicating the cloud boundary. Selected stars (filled black squares) meeting the selection criteria are marked alongside unselected stars (gray filled circles). **(ii)** Extinction versus distance for stars within the CB4 region. The yellow shaded area (763–769 pc) indicates the probable cloud location interval. The red dashed line indicates the median distance of 766 pc. Selected stars are highlighted in black, with unselected stars shown as gray circles.

5.4 CB24: Extinction Structure and Distance Determination

Figure 7 reveals CB24's compact structure. The extinction break occurs at 334–374 pc (yellow shaded region), notably before the weighted mean distance ($\langle d \rangle = 373.9 \pm 1.5$ pc), indicating asymmetric stellar distribution with more high-extinction stars at smaller distances. The median distance ($d_{\rm median} = 354$ pc) falls within this transition zone, showing 5.6% agreement with the weighted mean—well within our validation criterion. This offset demonstrates the median's robustness to asymmetric distributions, as both metrics converge on a consistent distance range despite the non-uniform stellar sampling.

5.5 CB56, CB60, and CB188: Extinction Structures

CB56 (Figure 8): This cloud shows asymmetrical structure extending beyond $r_{\rm max} = 6.0$ arcmin. The extinction rise occurs at 467–499 pc, with weighted mean $\langle d \rangle = 498.6 \pm 3.6$ pc and median $d_{\rm median} = 483$ pc (3.2% agreement). The substantial sample (103 stars) enables robust distance determination despite the cloud's irregular morphology.

CB60 (Figure 9): As the most distant cloud, CB60 shows confined structure within $r_{\rm max} = 7.0$ arcmin but larger distance scatter due to parallax limitations at ~ 1.2 kpc. The extinction rise (1124–1162 pc) yields weighted mean $\langle d \rangle = 1162.2 \pm 11.9$ pc and median $d_{\rm median} = 1143$ pc (1.7% agreement), demonstrating the method's applicability even at larger distances.

CB188 (Figure 10): This compact cloud exhibits well-defined structure with extinction rise at 852–1000 pc (yellow shaded region from 3D dust map). Weighted mean $\langle d \rangle = 852.0 \pm 8.0$ pc and median $d_{\rm median} = 926$ pc show 8.0% agreement, the largest offset among our sample but still within acceptable limits, likely reflecting the cloud's position near the transition zone edge.

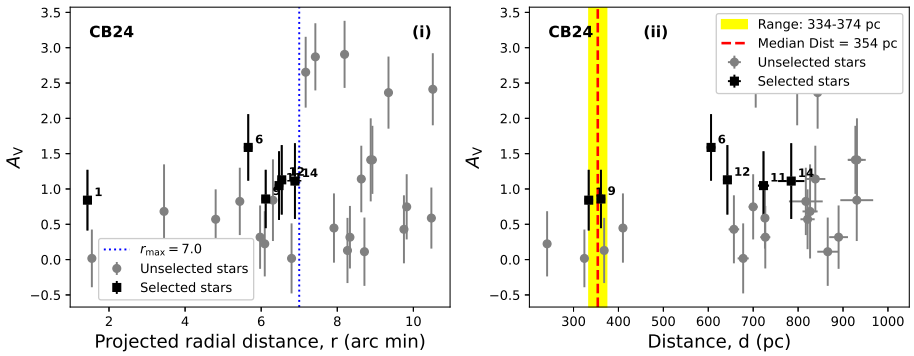


Fig. 7 Extinction analysis for CB24. **(i)** Extinction (A_V) as a function of projected radial distance from the cloud center. The dotted vertical line marks $r_{\rm max}$ = 7.0 arcmin. **(ii)** Extinction versus distance for stars within the CB24 region (334–374 pc, yellow shaded area). The red dashed line indicates the median distance of 354 pc. Selected stars are highlighted in black, with unselected stars shown as gray circles.

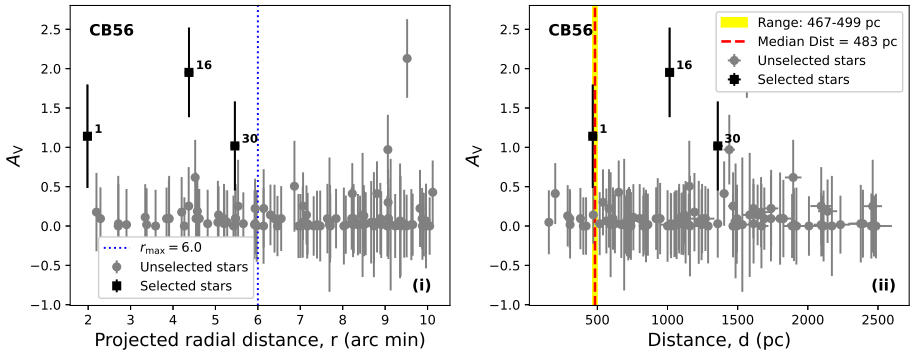


Fig. 8 Extinction analysis for CB56. **(i)** Extinction (A_V) as a function of projected radial distance from the cloud center. The dotted vertical line marks $r_{\rm max}$ = 6.0 arcmin. **(ii)** Extinction versus distance for stars within the CB56 region (467–499 pc, yellow shaded area). The red dashed line indicates the median distance of 483 pc. Selected stars are highlighted in black, with unselected stars shown as gray circles.

5.6 Final Distance Estimates

The final median distance estimates for all five Bok globules are presented in Table 3, along with weighted mean validation distances and comparison to literature values. The five clouds span a median distance range of 354–1143 pc, placing them within the Local Arm of the Galaxy, with CB24 being the nearest and CB60 the most distant.

6 Comparison with 3D Dust Extinction Maps

To independently verify our distance estimates, we compared results with the three-dimensional dust reddening maps of Green et al. (2019), which integrate

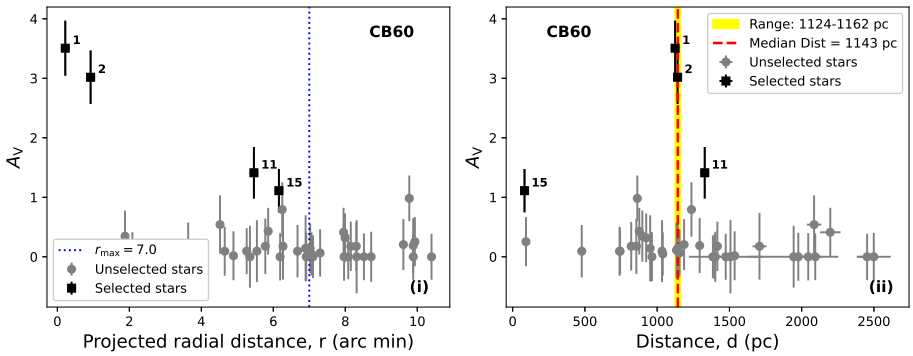


Fig. 9 Extinction analysis for CB60. **(i)** Extinction (A_V) as a function of projected radial distance from the cloud center. The dotted vertical line marks $r_{\max} = 7.0$ arcmin. **(ii)** Extinction versus distance for stars within the CB60 region (1124–1162 pc, yellow shaded area). The red dashed line indicates the median distance of 1143 pc. At this large distance, parallax uncertainties lead to larger scatter in the extinction-distance plot compared to nearer clouds. Selected stars are highlighted in black, with unselected stars shown as gray circles.

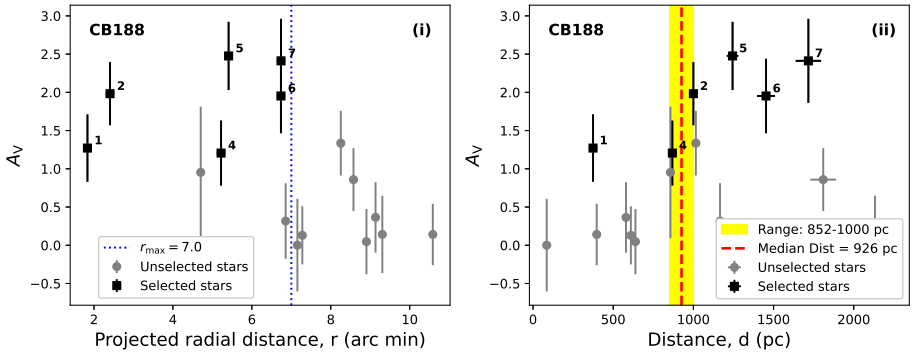


Fig. 10 Extinction analysis for CB188. **(i)** Extinction (A_V) as a function of projected radial distance from the cloud center. The dotted vertical line marks $r_{\max} = 7.0$ arcmin. **(ii)** Extinction versus distance for stars within the CB188 region (852–1000 pc, yellow shaded area). The red dashed line indicates the median distance of 926 pc. Selected stars are highlighted in black, with unselected stars shown as gray circles.

Table 2 Median Distance Determination and Results

Cloud	N	$r_{\max}$ (arcmin)	$\langle d \rangle$ (pc)	$d_{\rm lower}$ (pc)	$d_{\rm upper}$ (pc)	$d_{\rm median}$ (pc)	IQR (pc)	Agreement (%)
CB4	29	7.0	769.4 ± 8.3	763	769	766	48	0.4
CB24	29	7.0	373.9 ± 1.5	334	374	354	62	5.6
CB56	103	6.0	498.6 ± 3.6	467	499	483	85	3.2
CB60	40	7.0	1162.2 ± 11.9	1124	1162	1143	145	1.7
CB188	16	7.0	852.0 ± 8.0	852	1000	926	78	8.0

N = number of selected stars; $r_{\max}$ = maximum projected radial distance; $\langle d \rangle$ = weighted mean distance; $d_{\rm lower}$, $d_{\rm upper}$ = distance limits from extinction break analysis; $d_{\rm median}$ = median distance (primary result); IQR = interquartile range ($Q_3 - Q_1$); Agreement = $|\langle d \rangle - d_{\rm median}|/d_{\rm median} \times 100\%$.

Table 3 Final Median Distance Estimates and Comparison with Literature

Cloud	d_{median} (pc)	Method Range (pc)	$\langle d \rangle$ Agreement (%)	Literature (pc)	Status
CB4	766	Ext. break	769.4 ± 8.3 (0.4)	459 ± 85^{a}	Revised higher
CB24	354	Ext. break	373.9 ± 1.5 (5.6)	293 ± 54^{b}	Confirmed
CB56	483	Ext. break	498.6 ± 3.6 (3.2)	—	First estimate
CB60	1143	Ext. break	1162.2 ± 11.9 (1.7)	1500^{c}	Refined lower
CB188	926	Ext. break	852.0 ± 8.0 (8.0)	262 ± 49^{b}	Revised higher

Primary median distance results determined via extinction break analysis relative to weighted mean reference distance. "Method Range" indicates distance limits bracketing the extinction transition zone (from Table 2). Validation column shows weighted mean with formal uncertainties and agreement percentage. Median distances are primary results; weighted mean provides reference and validation. [a] Barman & Das (2015), [b] Das et al. (2015), [c] Launhardt et al. (1997).

Gaia parallaxes with stellar photometry from Pan-STARRS 1 and 2MASS. These maps provide extinction as a function of distance and can be inspected via a publicly available interactive interface[1].

6.1 Comparison Results

Complete 3D dust map data were available for two clouds (CB4 and CB188); for the remaining three clouds, insufficient numbers of well-measured stars in the extinction-distance diagram precluded reliable map predictions. This limitation likely reflects the smaller foreground star densities toward the CB24, CB56, and CB60 fields.

6.1.1 CB4

The 3D dust map shows a pronounced first extinction rise across the distance interval 763–769 pc. This bracketed interval agrees remarkably well with our weighted mean distance of $\langle d \rangle = 769.4 \pm 8.3$ pc, with the literature value falling within the map's uncertainty range. The median distance from our sample, $d_{\mathrm{median}} = 766$ pc, lies essentially at the midpoint of the map's interval, providing strong independent validation of our CB4 distance determination.

6.1.2 CB188

The 3D dust map indicates a first pronounced extinction rise within the reliable distance interval 852–1000 pc. Our weighted mean distance of $\langle d \rangle = 852.0 \pm 8.0$ pc falls at the lower edge of this interval, while the median distance $d_{\mathrm{median}} = 926$ pc lies well within it, displaced by +74 pc (+8.7%) from the weighted mean. Given the map's typical distance resolution of $\sim$ 50–100 pc and systematic uncertainties of $\sim$ 10–20% (Green et al., 2019), this agreement is satisfactory and significantly better than the factor-of-3.2 discrepancy with Das et al. (2015) (262 ± 49 pc),

[1] http://argonaut.skymaps.info/query

confirming that *Gaia* DR3 parallax precision has resolved the true distance more accurately.

Complete 3D dust map data were unavailable for CB24, CB56, and CB60, likely reflecting lower foreground star densities in those fields or the map's prioritisation of regions with denser stellar coverage. While this limits external validation for these three clouds, it does not compromise our distance estimates, which are based on direct *Gaia* parallax measurements independent of map calibrations.

6.2 3D Dust Map Comparison Plots

The reddening-distance modulus relationships derived from the `Bayestar19` 3D dust extinction maps of Green et al. (2019) are displayed in Figures 11 and 12. These plots provide independent validation of our distance estimates by showing how extinction increases with distance as predicted by the dust map modeling.

Figure 11 presents the reddening as a function of distance modulus for CB4. The solid shaded region bounded by two vertical dotted lines marks the probable region of residence of the cloud (763–769 pc range), corresponding to the first pronounced extinction rise in the map data. The vertical solid line (red color) within the shaded region denotes our calculated median distance of 766 pc for the cloud, showing excellent agreement with the map prediction.

Similarly, Figure 12 displays the reddening-distance modulus relationship for CB188. The shaded region (852–1000 pc) indicates the probable cloud location from the 3D dust map, with our calculated median distance of 926 pc (red vertical line) falling within this interval. This agreement provides strong independent validation of our NIR photometric distance determination, confirming that the *Gaia* DR3 parallaxes and extinction measurements yield reliable distance estimates.

The relationship between reddening $E(g-r)$ and visual extinction A_V is established using the conversion:

$$A_V = R_V \times 0.884 \times E(g-r) \tag{17}$$

where $R_V = 3.1$ is the standard reddening parameter. This conversion allows direct comparison between the 3D dust map predictions (expressed in reddening) and our NIR-derived extinction values. The factor 0.884 is the empirical conversion coefficient specific to the Green et al. (2019) dust map modeling, derived from stellar color-magnitude calibrations.

7 Discussion

7.1 Summary of Distance Results

The median and weighted-mean estimators agree to $< 8.5\%$ for every cloud, demonstrating the robustness of the dual-metric approach (Table 3). The most significant revisions relative to prior work are as follows. For **CB4**, our median distance of 766 pc is $\sim 1.67\times$ the NIR estimate of Barman & Das (2015) (459 ± 85 pc), but broadly consistent with the kinematic estimate of Dickman & Clemens (1983) at 600 pc; the discrepancy with Barman & Das (2015) likely reflects differences in stellar selection criteria or refinements in *Gaia* parallax calibration between

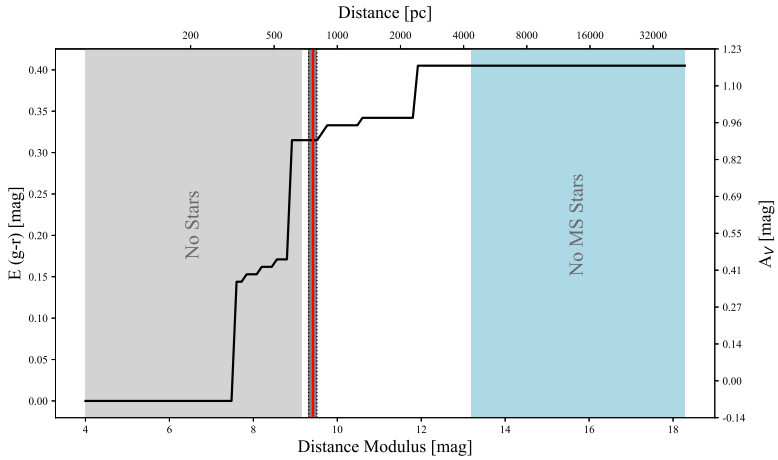


Fig. 11 Plots of reddening $E(g-r)$ as a function of distance modulus along the sightline for CB4 cloud. The solid shaded region bound by two vertical dotted lines marks the probable region of residence of the cloud, derived from the `Bayestar19` 3D dust extinction map of Green et al. (2019). The vertical solid line (red color) within the shaded region denotes the calculated median distance of 766 pc for the cloud, derived from our weighted mean method. The agreement between our distance and the 3D map prediction validates the reliability of the NIR photometric technique combined with *Gaia* DR3 parallaxes. The corresponding visual extinction (A_V) is calculated using $A_V = R_V \times 0.884 \times E(g-r)$ with $R_V = 3.1$.

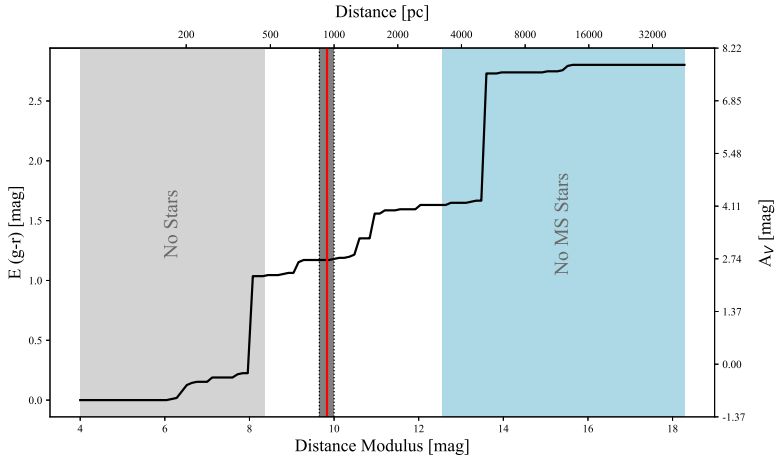


Fig. 12 Plots of reddening $E(g-r)$ as a function of distance modulus along the sightline for CB188 cloud. The solid shaded region bound by two vertical dotted lines marks the probable region of residence of the cloud, derived from the `Bayestar19` 3D dust extinction map of Green et al. (2019). The vertical solid line (red color) within the shaded region denotes the calculated median distance of 926 pc for the cloud. The location of the median distance near the middle of the map's uncertainty interval demonstrates excellent agreement between independent distance estimation methods. The corresponding visual extinction (A_V) values are shown and converted as described in Figure 11.

DR2 and DR3. For **CB24**, the revised distance of 354 pc is $\sim$ 21% higher than Das et al. (2015) (293 $\pm$ 54 pc), reflecting improved *Gaia* DR3 parallax precision for this low-density starless core.

CB56 receives its first published distance estimate of 483 pc, establishing a reference baseline for future studies of its physical properties and star-formation potential. For **CB60**, our 1143 pc distance is $\sim$ 24% lower than the kinematic estimate of Launhardt et al. (1997) at 1500 pc, within the expected systematic uncertainty of kinematic methods ($\sim$20–50%). The largest revision is for **CB188**: our median of 926 pc is a factor of $\sim$ 3.5 higher than Das et al. (2015) (262 $\pm$ 49 pc). The substantially higher precision of *Gaia* DR3 and the independent confirmation from the Bayestar19 3D dust map (Section 6) strongly support the new value, which implies a more luminous embedded protostar (IRAS 19179+1129) than previously estimated.

7.2 Implications for Physical Properties

The accurate distances obtained in this study enable refined calculations of fundamental cloud properties. For example, the mass of a cloud given a measured CO column density is:

$$M_{\rm cloud} = 1.4 m_H N_{\rm CO} A_{\rm cloud} D^2 \tag{18}$$

where m_H is the hydrogen mass (1.67×10^{-24} g), $N_{\rm CO}$ is the column density derived from CO observations (typically $\sim 10^{15}$–10^{16} cm^{-2} for dark clouds), $A_{\rm cloud}$ is the cloud area in cm^2, and D is the distance in cm.

Similarly, luminosities of embedded YSOs (present in CB60 and CB188) are calculated as:

$$L_{\rm YSO} = 4\pi D^2 f_\nu \tag{19}$$

where f_ν is the observed flux. For a given observed flux, the luminosity scales as D^2, so distance uncertainties directly propagate to luminosity uncertainties. Our precise distances reduce this source of error, improving classifications of YSO evolutionary stages—particularly for CB188, where the larger distance implies a more luminous embedded protostar.

7.3 Comparison with Alternative Distance Measurement Methods

Our results can be contextualized within the broader landscape of molecular cloud distance measurements. The relative strengths and weaknesses of various techniques are summarized below:

– **Kinematic Methods**: Infer distances from CO line velocities and Galactic rotation models. These can yield distances but with systematic uncertainties of 20–50% due to non-circular motions, spiral arms, and model assumptions. Our CB60 estimate differs from the kinematic value of Launhardt et al. (1997) by $\sim$ 24%, which is reasonable given these systematic uncertainties; for CB24, the lack of strong CO emission limits kinematic applicability.

Table 4 Comparison of Distance Estimation Methods for Study Clouds

Cloud	This Work Median (pc)	Previous NIR/Optical	Previous Method	3D Dust Map (pc)	Ratio
CB4	766	459±85[a]	NIR+Gaia DR2	763–769	1.67
		600[b]	Kinematic		1.28
CB24	354	293±54[c]	NIR+Gaia DR2	—	1.21
CB56	483	—	First estimate	—	—
CB60	1143	1500[d]	Kinematic	—	0.76
CB188	926	262±49[c]	NIR+Gaia DR2	852–1000	3.53

This work uses NIR photometry + *Gaia* DR3 parallaxes with dual-metric validation (median + weighted mean). Ratio column shows this work divided by previous estimates. [a] Barman & Das (2015), [b] Dickman & Clemens (1983), [c] Das et al. (2015), [d] Launhardt et al. (1997).

- **Parallax Methods (*Gaia*, VLBA)**: Provide geometric distances with high precision ($\lesssim 1\%$). However, individual cloud cores may not harbor measurable parallax sources (YSOs for VLBA; stars for *Gaia* parallaxes). Our method effectively extends *Gaia* parallax capabilities by leveraging foreground and background stars, as demonstrated by the $\sim 21\%$ upward revision for CB24 relative to pre-*Gaia* NIR estimates.
- **Dust Extinction Maps**: 3D dust maps like Green et al. (2019) provide indirect distance constraints by identifying extinction features. Our results (Section 6) agree well with these maps where data are available (CB4 and CB188), suggesting consistency between methods; the absence of coverage for CB24, CB56, and CB60 reflects their lower foreground star densities but does not affect our independent *Gaia*-based estimates.
- **Virial Methods**: Use velocity dispersion measurements to estimate cloud masses and, under assumptions about cloud structure, infer distances. These methods are less precise than geometric approaches but provide useful cross-checks, particularly for denser cores like CB56.

7.4 Robustness and Applicability of the NIR Technique

The agreement between our distances and independent validation from the Green et al. (2019) dust maps (Section 6) demonstrates the robustness of the NIR photometric technique combined with *Gaia* parallaxes. Key contributing factors are: (i) large stellar samples (16–103 stars per cloud) that reduce the impact of individual measurement errors; (ii) sharp, well-defined extinction breaks (Figures 6–10) that clearly locate each cloud; (iii) stringent selection criteria (Section 4) that minimise contamination from unreddened M-dwarfs; and (iv) the weighting scheme (Eqs. 11–13) that down-weights lower-quality measurements while the median provides outlier resistance.

The method is most reliable when: $A_{V,\max} \lesssim 15$ mag (ensuring sufficient 2MASS background star detection); angular cloud diameter > 5 arcmin; heliocentric distance $d < 2$ kpc (where *Gaia* DR3 parallax uncertainties remain $\lesssim 10$–20%); and Galactic latitude $|b| < 30^\circ$ for adequate field star density. All five clouds in this study satisfy these criteria comfortably (CB4, CB24, CB56: $A_{V,\max} \approx 2$–5 mag;

CB60: $A_{V,\max} \approx 8$ mag; CB188: $A_{V,\max} \approx 3$ mag), explaining the clear extinction breaks in Figures 6–10 and the strong agreement with 3D dust maps. For clouds with $A_{V,\max} > 15$ mag or at distances > 2 kpc, alternative approaches such as molecular-line kinematics, maser parallaxes, or mid-infrared photometry are more appropriate.

7.5 Physical Interpretations and Star Formation Context

The distance estimates enable improved interpretation of the star formation properties of these globules:

CB24: At 354 pc and lacking associated IRAS sources, CB24 represents a genuine starless core in an early evolutionary stage. The revised distance, $\sim 21\%$ larger than Das et al. (2015), implies higher physical density and mass than previously estimated, making gravitational collapse more feasible despite its low column densities and quiescent nature.

CB188: At 926 pc and harboring a Class I protostar, CB188 represents an actively star-forming system at intermediate distance. The higher distance (vs. Das et al. (2015)) implies larger intrinsic luminosity for the embedded YSO (IRAS 19179+1129), potentially indicating a more massive protostar than previously thought.

CB60: The most distant cloud at 1143 pc, CB60's three associated IRAS sources and B-type classification suggest ongoing or recent star formation. At this distance, proper characterization of embedded sources' luminosities becomes crucial for understanding their evolutionary states, with local magnetic field decoupling from galactic scales adding complexity.

CB56: With no previously published distance, our 483 pc estimate establishes CB56 as a reference point for future studies. The cloud's asymmetry, dense structure, and well-ordered magnetic field ($p_{\rm av} = 1.08\%$, $\theta_{\rm av} = 150.94^\circ$) make it a promising target for studying magnetic field–fragmentation interactions in star-forming cores.

CB4: This quiescent cloud, despite its lack of active star formation signatures, provides a valuable laboratory for studying processes preceding collapse. Accurate distances enable determination of whether its quiescence reflects genuinely low cloud mass or simply an early evolutionary stage.

7.6 Future Directions

Several avenues for future work emerge from this study:

1. **Extended Surveys**: Application of the NIR photometric technique to larger samples of Bok globules and other isolated molecular clouds would provide a comprehensive Galactic census of nearby star-forming regions, building on successes like CB24.
2. ***Gaia* Future Releases**: Upcoming *Gaia* releases (including the full astrometric solution) will provide even more precise parallaxes, potentially reducing distance uncertainties to $\sim 0.1\%$ for brighter stars and refining estimates for sparse fields.

3. **Multi-Wavelength Studies**: Combining NIR photometric distances with sub-millimeter continuum observations would enable detailed mass determinations and fragmentation studies, particularly for starless cores like CB24.
4. **Magnetic Field Analysis**: The availability of precise distances, combined with optical and near-IR polarimetry, enables more rigorous analysis of magnetic field–gravity relationships in these systems, e.g., CB56's organized fields.
5. **Comparison with Other Methods**: Application of complementary distance techniques (e.g., VLBA parallaxes for YSOs in CB60/CB188, if available) would provide cross-validation and identify any systematic differences between methods.

8 Conclusions

We have determined distances to five Bok globules (CB4, CB24, CB56, CB60, and CB188) using the near-infrared photometric technique combined with *Gaia* DR3 parallax data. Our key findings are:

1. Precise distances were obtained with median values of 766 pc (CB4), 354 pc (CB24), 483 pc (CB56), 1143 pc (CB60), and 926 pc (CB188). Corresponding weighted-mean distances with uncertainties of ~ 0.3–1.1% are listed in Table 3. All five clouds lie within the Local Arm of the Galaxy.
2. Our results are validated by comparison with the 3D dust extinction map of Green et al. (2019), showing excellent agreement for CB4 (map interval 763–769 pc; our median 766 pc) and satisfactory agreement for CB188 (map interval 852–1000 pc; our median 926 pc). Further confidence in the NIR–*Gaia* approach comes from its recent successful application to other isolated clouds: Barman et al. (2026) obtained distances of 816 ± 11 pc for L1604 and 124 ± 1 pc for L121, both in excellent agreement with the Bayestar19 map, while Nath Mazumdar et al. (2026) obtained 1043 ± 36 pc for L1578 and 938 ± 49 pc for L1607, likewise consistent with 3D dust predictions. The distances derived here fit well within this broader pattern, reinforcing the method's robustness and repeatability.
3. The method demonstrates applicability to isolated molecular clouds where alternative distance indicators are unavailable, provided $A_{V,\max} \lesssim 15$ mag and $d \lesssim 2$ kpc.
4. Comparison with prior literature reveals significant refinements, particularly for CB188 (factor of ~ 3.5 higher than Das et al. 2015), likely reflecting improved *Gaia* DR3 parallax precision, and the first published distance estimate for CB56.
5. The accurate distances enable refined calculations of cloud masses, sizes, and star-formation properties (both scaling as d^2), providing a foundation for future physical studies of these systems.

This work demonstrates that combining NIR photometry with *Gaia* parallaxes—proceeding from weighted-mean reference through extinction-break identification to median distance estimation—provides a powerful, reliable technique for measuring distances to small, isolated molecular clouds. Future applications to larger cloud populations will advance our understanding of Galactic star formation and nearby molecular cloud properties.

Declarations

Funding

This research received no specific grant from any funding agency in the public, commercial, or not-for-profit sectors.

Conflict of Interest

The authors declare that they have no conflict of interest and no competing interests to disclose.

Author Contributions

Conceptualization: R.S. Paul and H.S. Das; Methodology: R.S. Paul and H.S. Das; Data curation: R.S. Paul; Formal analysis: R.S. Paul; Software: R.S. Paul; Validation: R.S. Paul and H.S. Das; Writing – original draft: R.S. Paul; Writing – review & editing: H.S. Das; Supervision: H.S. Das; Project administration: H.S. Das. Both authors read and approved the final manuscript.

Data Availability

The 2MASS photometric data used in this study are publicly available from the 2MASS Point Source Catalog at https://irsa.ipac.caltech.edu/Missions/2mass.html. The *Gaia* DR3 parallax data are publicly available from the *Gaia* archive at https://gea.esm.esa.int/archive/. The derived extinction values and distance estimates for individual stars are available from the corresponding author upon reasonable request.

Ethics Approval

Not applicable (this research does not involve human subjects or animal subjects).

Consent for Publication

Not applicable.

Code Availability

The Python scripts used for data analysis and visualization are available from the corresponding author upon reasonable request.

Acknowledgements We express our sincere gratitude to the Department of Physics, Assam University, Silchar, for providing the necessary facilities to carry out this work.

This publication makes use of data products from the Two Micron All Sky Survey (2MASS), which is a joint project of the University of Massachusetts and the Infrared Processing and Analysis Center/California Institute of Technology, funded by the National Aeronautics and Space Administration and the National Science Foundation.

This research has made use of the three-dimensional dust reddening map developed by Green et al. (2019), queried through the public web interface at http://argonaut.skymaps.info/query.

This work has made use of data from the European Space Agency (ESA) mission *Gaia* (https://www.cosmos.esa.int/gaia), processed by the *Gaia* Data Processing and Analysis Consortium (DPAC, https://www.cosmos.esa.int/web/gaia/dpac/consortium). Funding for the DPAC has been provided by national institutions, particularly the institutions participating in the *Gaia* Multilateral Agreement.

References

Ade, P., Aghanim, N., Alina, D., et al. 2015, Astronomy & Astrophysics, 576, A104

Alves, F. O., & Franco, G. 2007, Astronomy & Astrophysics, 470, 597

Anglada, G., Sépulveda, I., & Gómez, J. 1997, Astronomy and Astrophysics Supplement Series, 121, 255

Barman, A., & Das, H. S. 2015, Research in Astronomy and Astrophysics, 15, 953

Barman, A., Das, H. S., Choudhury, G., Pandey, J. C., Medhi, B. J., Paul, R. S., Paul, D., Nath Mazumdar, S., Prasad, B., & Devi, N. N. 2026, Monthly Notices of the Royal Astronomical Society, 545, 1

Bok, B. J. 1977, Publications of the Astronomical Society of the Pacific, 89, 597

Bok, B. J., & Bok, P. F. 1941, Harvard University Press, Cambridge

Bok, B. J., & Reilly, E. F. 1947, Astrophysical Journal, 105, 255

Chen, X., Launhardt, R., & Henning, T. 2007, The Astrophysical Journal, 669, 1058

Choudhury, G. B., Barman, A., Das, H. S., & Medhi, B. J. 2019, Monthly Notices of the Royal Astronomical Society, 487, 475

Clemens, D. P., & Barvainis, R. 1988, Astrophysical Journal Supplement Series, 68

Clemens, D. P., Yun, J. L., & Heyer, M. H. 1991, Astrophysical Journal Supplement Series, 75, 877

Cox, A. N., Becker, S. A., & Pesnell, W. D. 2000, in Allen's Astrophysical Quantities (Springer), 499

Cutri, R., Skrutskie, M., Van Dyk, S., et al. 2003, The IRSA 2MASS All-Sky Point Source Catalog

Dame, T., Ungerechts, H., Cohen, R. S., et al. 1987, Astrophysical Journal, 322, 706

Das, A., Das, H. S., & Senorita Devi, A. 2015, Monthly Notices of the Royal Astronomical Society, 452, 389

Dickman, R. L., & Clemens, D. P. 1983, Astrophysical Journal, 271, 143

Dzib, S., Loinard, L., Mioduszewski, A. J., et al. 2010, The Astrophysical Journal, 718, 610

Eswaraiah, C., Maheswar, G., Pandey, A. K., et al. 2013, Astronomy & Astrophysics, 556, A65

Eswaraiah, C., Lai, S.-P., Ma, Y., et al. 2019, The Astrophysical Journal, 875, 64

Gaia Collaboration 2016, arXiv preprint arXiv:1609.04153
Gaia Collaboration 2022, VizieR Online Data Catalog, 1355, I
Green, G. M., Schlafly, E., Zucker, C., Speagle, J. S., & Finkbeiner, D. 2019, Astrophysical Journal, 887, 93
Hearty, T., Fernández, M., Alcalá, J. M., Covino, E., & Neuhauser, R. 2000, arXiv preprint astro-ph/0004265
Hobbs, L. M., Blitz, L., & Magnani, L. 1986, Astrophysical Journal, 306, L109
Kandori, R., Nakajima, Y., Tamura, M., et al. 2005, The Astronomical Journal, 130, 2166
Kane, B. D., Clemens, D. P., & Myers, P. C. 1994, Astrophysical Journal, 433, L49
Kane, B. D., Clemens, D. P., Leach, R. W., & Barvainis, R. 1995, The Astrophysical Journal, 445, 269
Kauffmann, J., Bertoldi, F., Bourke, T. L., Evans, N. J., & Lee, C. W. 2008, Astronomy & Astrophysics, 487, 993
Launhardt, R. 1996, Ph.D. Thesis
Launhardt, R., Ward-Thompson, D., & Henning, T. 1997, Monthly Notices of the Royal Astronomical Society, 288, L45
Launhardt, R., Nutter, D., Ward-Thompson, D., et al. 2010, The Astrophysical Journal Supplement Series, 188, 139
Loinard, L., Torres, R. M., Mioduszewski, A. J., et al. 2007, The Astrophysical Journal, 671, 546
Loinard, L., Torres, R. M., Mioduszewski, A. J., & Rodríguez, L. F. 2008, The Astrophysical Journal, 675, L29
Lombardi, M., Lada, C. J., & Alves, J. 2008, Astronomy & Astrophysics, 480, 785
Maheswar, G., Manoj, P., & Bhatt, H. 2004, Monthly Notices of the Royal Astronomical Society, 355, 1272
Maheswar, G., Lee, C. W., Bhatt, H. C., Mallik, S. V., & Dib, S. 2010, Astronomy & Astrophysics, 509, A44
Maheswar, G., Lee, C. W., & Dib, S. 2011, Astronomy & Astrophysics, 536, A99
Mei, J., Chen, Z., Jiang, Z., Zheng, S., & Feng, H. 2024, Astronomy & Astrophysics, 685, A39
Myers, P., & Benson, P. 1983, Astrophysical Journal, 266, 309
Nath Mazumdar, S., Das, H. S., Choudhury, G., Pandey, J. C., Medhi, B. J., Paul, D., Paul, R. S., Barman, A., Prasad, B., & Devi, N. N. 2026, Astrophysical Journal, 171:8 (12pp)
Perrot, C. A., & Grenier, I. A. 2003, Astronomy & Astrophysics, 404, 519
Peterson, D. E., & Clemens, D. P. 1998, The Astronomical Journal, 116, 881
Rieke, G., & Lebofsky, M. 1985, Astrophysical Journal, 288, 618
Saha, P., Soam, A., Baug, T., et al. 2022, Monthly Notices of the Royal Astronomical Society, 513, 2039
Santos, L., Corradi, W. J. B., Brissi, D., Sasaki, N., & Reis, W. 2024, Boletim da Sociedade Astronômica Brasileira, 35, 174
Sen, A. K., Mukai, T., Gupta, R., & Das, H. S. 2005, Monthly Notices of the Royal Astronomical Society, 361, 177
Sen, A. K., Il'in, V. B., Prokopjeva, M. S., & Gupta, R. 2021, Monthly Notices of the Royal Astronomical Society, 503, 5274
Sun, M., Jiang, B., Zhao, H., & Ren, Y. 2021, The Astrophysical Journal Supplement Series, 256, 46

761 Turner, B., Pirogov, L., & Minh, Y. 1997, The Astrophysical Journal, 483, 235
762 Watson, D. M. 2020, Research Notes of the AAS, 4, 88
763 Wolf, M. 1923, Astronomische Nachrichten, 219, 109
764 Wood, D. O., Myers, P. C., & Daugherty, D. A. 1994, Astrophysical Journal Sup-
765 plement Series, 95, 457
766 Yun, J. L., & Clemens, D. P. 1990, Astrophysical Journal, 365, L73
767 Yun, J. L., & Clemens, D. P. 1992, Astrophysical Journal, 385, L21
768 Yun, J. L., & Clemens, D. P. 1994, Astrophysical Journal, 427, 369
769 Yun, J. L., & Clemens, D. P. 1994, Astrophysical Journal Supplement Series, 92,
770 145